Notch-fatigue Strength of Advanced TRIP-aided Martensitic Steels

Junya KOBAYASHI,[1]* Nobuo YOSHIKAWA[2] and Koh-ichi SUGIMOTO[3]

1) Research Fellow of Japan Society for the Promotion of Science, Graduate Student, Shinshu University, 4-17-1 Wakasato, Nagano, 380-8553 Japan.   2) Graduate Student, Shinshu University, 4-17-1 Wakasato, Nagano, 380-8553 Japan.
3) Department of Mechanical Systems Engineering, Shinshu University, 4-17-1 Wakasato, Nagano, 380-8553 Japan.

The notch-fatigue limit and notch sensitivity of 0.1–0.6%C-1.5%Si-1.5%Mn *transformation-induced plasticity (TRIP)-aided martensitic steels* (*TM steels*) were investigated for use as common rails in next-generation automotive diesel engines. Also, these properties were related to the microstructural and retained austenite characteristics. When TM steels containing 0.2% to 0.4% C were subjected to heat treatment for isothermal transformation at 50°C and subsequent partitioning at 250°C, the steels achieved much higher notch-fatigue limits and lower notch sensitivities than those of conventional 0.2–0.4%C-1.0%Cr-0.2%Mo structural steels. This was principally associated with (i) plastic relaxation of localized stress concentration as a result of strain-induced transformation of 3–5 vol% metastable retained austenite and (ii) a large amount of finely dispersed martensite-austenite phase along prior austenitic, packet and block boundaries, as well as (iii) a small amount of carbide only in the wide lath-martensite structure, which may contribute to making fatigue crack initiation and/or propagation difficult.

KEY WORDS: notch-fatigue strength; notch sensitivity; ultrahigh-strength steel; TRIP-aided steel; martensite; retained austenite; M-A constituent.

1. Introduction

For the past decade, second- and third-generation advanced high-strength steels such as 5–25%Mn transformation-induced plasticity (TRIP)/twinning-induced plasticity steels,[1–3] C–Si–Mn quench and partitioning steels,[4] and C–Si–Mn TRIP-aided bainitic ferrite (TBF) steels[5,6] have been developed to reduce the weight of automotive bodies in white and to improve impact safety. In order to enhance the tensile strength further, C–Si–Mn ultrahigh-strength TRIP-aided steels with a martensitic matrix (*TRIP-aided martensitic steel; TM steel*)[7–9] have recently been developed for automotive applications. These TM steels can be produced by an isothermal transformation (IT) process below the martensite-finish temperature (M_f) after austenitizing and a subsequent partitioning (P) process at temperatures below 350°C (hereafter a combination of the IT and P processes is called an ITP process). Resultantly, the TM steels are characterized not only by good sheet formability, but also by high impact toughness[10] and fracture toughness.[11] If the TM steel possesses a high notch-fatigue strength, it has potential applications such as in precision driving parts and in ultrahigh-pressure common rails for diesel engines. However, such a notch-fatigue strength has not yet been investigated.

In the present study, the notch-fatigue properties of 0.1–0.6%C-1.5%Si-1.5%Mn TM steels were investigated and compared with those of commercial Cr–Mo-containing structural steels (SCM420, SCM435 and SCM440 steels). In addition, the notch-fatigue limit and notch sensitivity were related to metallurgical factors such as microstructural and retained austenite characteristics.

2. Experimental Procedure

In the current work, five kinds of steel bars, A–E, with different carbon contents were prepared by vacuum melting, followed by hot forging and hot rolling to a diameter of 13 mm. The chemical compositions and estimated martensite-start temperatures (M_ss)[12] are listed in **Table 1**. For comparison, commercial SCM420 (steel F) and SCM435 (steel G) steel bars, and a vacuum-melted SCM440 (steel H) steel bar of diameter 13 mm were used.

After smooth and notched specimens for tension and fatigue tests (**Fig. 1**) were machined from these steel bars, the ITP process illustrated in **Fig. 2** (isothermal transformation at T_{IT} = 50°C and then partitioning at T_P = 250°C) was conducted in salt baths for steels A–E. Partitioning was conducted for further carbon-enrichment in the retained austenite. For steels F–H, quenching in oil at 50°C after austenitizing at 900°C and then tempering at 200 to 600°C for 3 600 s were carried out.

The retained austenite characteristics of steels A–E were investigated by X-ray diffractometry. The specimens were electro-polished after grinding with Emery paper (#1200). The volume fraction of retained austenite (f_γ, vol%) was quantified from the integrated intensity of the $(200)\alpha$, $(211)\alpha$, $(200)\gamma$, $(220)\gamma$ and $(311)\gamma$ X-ray diffraction peaks, using Mo–Kα radiation.[13] The carbon concentration (C_γ,

Table 1. Chemical compositions (mass%) and estimated martensite-start temperatures (Ms, °C) of steels used.

Steel		C	Si	Mn	P	S	Cr	Mo	Al	O	N	Ms
TM	A	0.10	1.49	1.50	0.015	0.0015	< 0.01	< 0.01	0.039	0.0007	0.0007	457
	B	0.20	1.51	1.51	0.015	0.0011	< 0.01	< 0.01	0.040	0.0012	0.0012	420
	C	0.29	1.50	1.50	0.014	0.0012	< 0.01	< 0.01	0.040	0.0014	0.0013	388
	D	0.40	1.49	1.50	0.015	0.0012	< 0.01	< 0.01	0.043	0.0015	0.0010	348
	E	0.61	1.50	1.53	0.015	0.0011	< 0.01	< 0.01	0.034	0.0009	0.0014	270
SCM	F	0.21	0.21	0.86	0.016	0.018	1.12	0.16	0.035	*	0.0031	416
	G	0.35	0.17	0.78	0.012	0.019	1.12	0.16	0.033	*	0.0029	369
	H	0.41	0.19	0.80	< 0.005	0.0009	1.00	0.20	0.044	0.0018	0.0009	351

*: not measured; TM: TRIP-aided martensitic steel; SCM: Cr–Mo bearing structural steel.
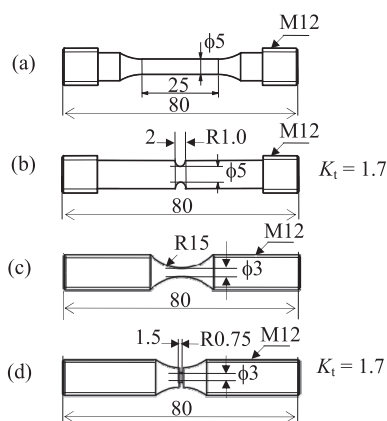

Fig. 1. Dimensions of (a, c) smooth and (b, d) notched specimens for (a, b) tensile and (c, d) fatigue tests. Notch root radii of (b) and (d) are 1 mm and 0.75 mm, respectively.
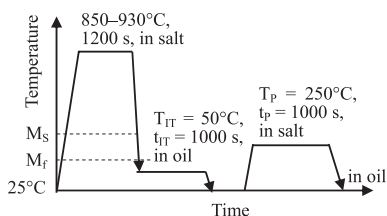

Fig. 2. Heat treatment diagram for steels A–E; T_{IT}, t_{IT}, T_P and t_P represent isothermal transformation temperature, isothermal transformation time, partitioning temperature and partitioning time, respectively.

Fig. 3. Sinusoidal curve of fatigue test. σ_R: stress amplitude, σ_{max}: maximum stress, σ_{min}: minimum stress. Stress ratio ($R = \sigma_{max}/\sigma_{min}$) is 0.1.

mass%) was estimated from the empirical equation[14] shown below. In this case, the lattice constant (a_γ, × 0.1 nm) was measured from the $(200)\gamma$, $(220)\gamma$ and $(311)\gamma$ peaks using Cu–Kα radiation.

$$a_\gamma = 3.5780 + 0.0330\%C_\gamma + 0.00095\%Mn_\gamma - 0.0002\%Ni_\gamma$$
$$+ 0.0006\%Cr_\gamma + 0.0220\%N_\gamma + 0.0056\%Al_\gamma - 0.0004\%Co_\gamma$$
$$+ 0.0015\%Cu_\gamma + 0.0031\%Mo_\gamma + 0.0051\%Nb_\gamma$$
$$+ 0.0039\%Ti_\gamma + 0.0018\%V_\gamma + 0.0018\%W_\gamma$$
$$\text{...} (1)$$

where $\%Mn_\gamma$, $\%Ni_\gamma$, $\%Cr_\gamma$, $\%N_\gamma$, $\%Al_\gamma$, $\%Co_\gamma$, $\%Cu_\gamma$, $\%Mo_\gamma$, $\%Nb_\gamma$, $\%Ti_\gamma$, $\%V_\gamma$ and $\%W_\gamma$ represent the concentrations of individual elements (mass%) in retained austenite. As an approximation, the added contents of the above alloying elements were substituted for these concentrations in this study.
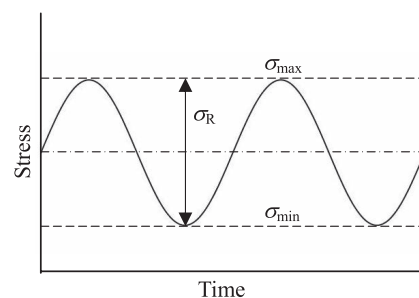
The microstructures of the steels were observed using a field-emission scanning electron microscope (FE-SEM) with electron backscattering diffraction (EBSD) system and a transmission electron microscope. Samples for FE-SEM-EBSD analysis taken from the grip section of the tensile and fatigue specimens were ground using colloidal silicon after alumina grinding. The volume fraction of the second phase was estimated from the SEM image and the image quality map from EBSD analysis. Vickers hardness tests were carried out using a micro Vickers hardness tester (load: 0.98 N) at 25°C.

The surfaces of all the specimens for tension and fatigue tests were ground using #600 Emery paper before testing. Tension tests were conducted using a tensile testing machine (AG-10TD; Shimadzu Co., Japan) at 25°C and at a crosshead speed of 1 mm/min. In order to measure precisely yield stress (0.2% offset proof stress), strain gauge (gauge length: 10 mm, Kyowa Electronic Instruments Co., Ltd) was attached on surface of specimen. The displacement was measured from the position of the cross head and the load was measured by the load cell. Fatigue tests were carried out using a multi-type fatigue testing machine (PMF4-10; Takes-Group Ltd., Japan) at 25°C, with a sinusoidal wave of 80 Hz. The stress ratio, defined as the ratio of minimum stress (σ_{min}) to maximum stress (σ_{max}) was $R = 0.1$ (**Fig. 3**). The fatigue limit was defined by the maximum value of the stress amplitude ($\sigma_R = \sigma_{max} - \sigma_{min}$) without failure up to 1.0×10^7 cycles.

3. Results

3.1. Microstructure and Retained Austenite Characteristics

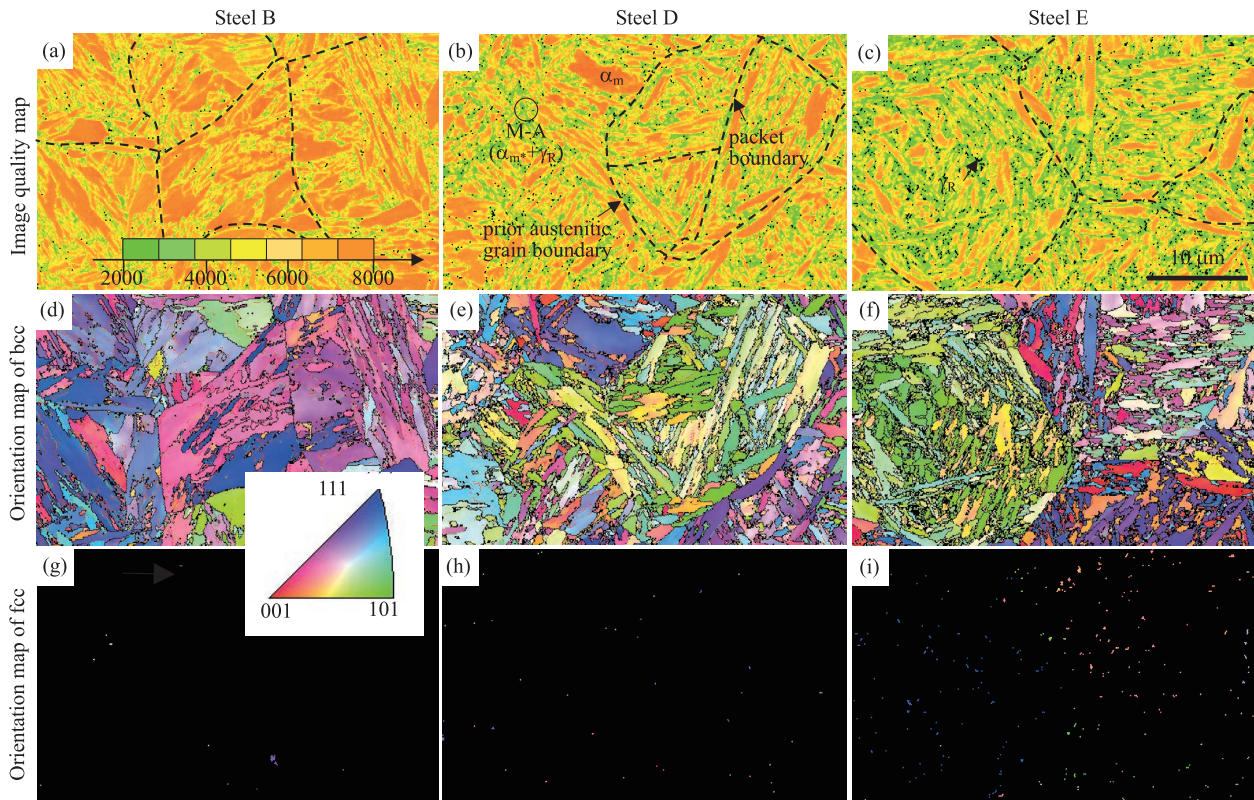**Figure 4** shows image quality (IQ) maps and orientation

Fig. 4. Image quality distribution maps of body-centered cubic (bcc) phase and orientation maps of bcc and face-centered cubic (fcc) phases in steels B, D, and E. In (a)–(c), α_m, α_m* and γ_R represent wide lath-martensite (dark yellow), narrow lath-martensite (yellowish green) and retained austenite (dotted black).

maps of steels B, D and E. The microstructures of steels B–E principally consist of a wide lath-martensite structure matrix or martensite block structure (dark-yellow phase) and a blocky second phase (yellowish-green phase) (Figs. 4(a)–4(c)), although the steel A possesses a large amount of polygonal ferrite located on the prior austenitic grain boundary because of its low hardenability. Steel C possesses the almost same microstructure of steel B. The blocky second phases of steels B–E, which are located on prior austenitic grain, packet and block boundaries, are characterized by lower IQ indexes, indicating that the second phases possess higher dislocation densities and/or finer microstructures.[15] With increasing carbon content, block size decreases and the blocky second phase fraction increases. Also, most of the retained austenite phases are very fine and exist mainly in the blocky second phase. The microstructures of steels F–H also consist of a wide lath-martensite structure matrix and a blocky second phase, like steel B–E. However, the steels F–H are characterized by an absence of the retained austenite.

As shown in **Fig. 5**(a), a large amount of fine and needle-shaped carbide seems to precipitate only in the wider lath-martensite structure. It is expected that the needle-shaped carbides are precipitated by auto-tempering on quenching. Most of the blocky second phases are found to consist of narrow lath-martensite structures and retained austenite (Fig. 5(b)). Although the retained austenite morphology in the blocky second phase is indistinct, it seems that the retained austenite, observed as a dotted phase in the second phase (Figs. 4(a)–4(c)) is located along the narrow lath-martensite boundary. These results suggest that the blocky second phase seems to a martensite-austenite constituent or
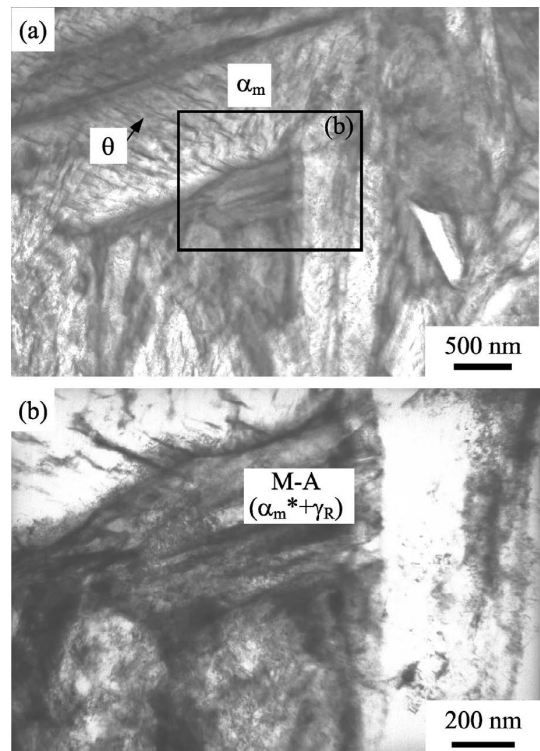

Fig. 5. Transition electron microscopy images of steel D, in which α_m, α_m*, γ_R and θ represent wide lath-martensite, narrow lath-martensite, retained austenite and carbide, respectively.

phase which is observed in martensitic steel of the prior studies.[9,16] Hereafter, the blocky second phase is called an "*M-A like phase*".

Figure 6 shows the variations in the initial volume fraction and carbon concentration of the retained austenite and volume fractions of the M-A like phase and carbide, as a function of the carbon content in steels A–E. It is seen in Fig. 6(a) that the carbon concentration reaches peak value in steels B and C. Note that the carbon concentrations in steels D and E are lower than the added carbon contents. In contrast, the volume fraction of retained austenite increases with increasing carbon content. In particular, steel E has a significant volume fraction of retained austenite.
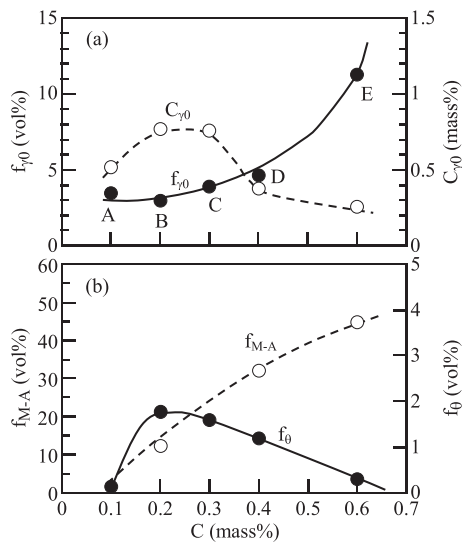
The volume fraction of the M-A like phase increases monotonically with increasing carbon content (Fig. 6(b)). However, the volume fraction of carbide becomes maximum in steel B, although the carbide fraction ($f_\theta = 1.77$ vol%) is much lower than that (4.20 vol%) in steel F.

3.2. Vickers Hardness and Tensile Properties

Figure 7 shows flow curves of smooth and notched specimens of steels A–E. **Table 2** shows the Vickers hardness and tensile properties of these steels. The Vickers hardness values of steels A–E are between HV284 and HV717, and increase with increasing carbon content. Similarly, both the yield stress or 0.2% offset proof stress and tensile strength increase with increasing carbon content. In contrast, the total elongation decreases with increasing carbon content, except for steel E.

The notch-tensile strength (TS_N) increases with increasing carbon content in the same way as the tensile strength (TS). As a result, steels B–D exhibit high notch-tensile strength ratios ($NSR = TS_N/TS$), except for steels A and E, although these notch-tensile strength ratios are somewhat lower than those of steels F–H.[17]

3.3. Notch-Fatigue Limit and Notch Sensitivity for Fatigue

Figure 8 shows stress amplitude-number of cycles (S–N) curves of steels A–E. **Figure 9** shows the fatigue limits of smooth and notched specimens and the "*notch sensitivity factor q*",[18] defined by the following equation:

$$q = (K_f - 1)/(K_t - 1) \quad\quad\quad\quad (2)$$

where K_f and K_t are the fatigue-notch factor ($= FL/FL_N$) and stress concentration factor (1.7 in this study), respectively.

The fatigue limits of both smooth and notched specimens increase linearly with carbon content (or Vickers hardness) in steels A–D. The notch sensitivity becomes minimum in steel C. When the notch-fatigue limits of steels B–D were compared with those of steels F–H, they were found to be higher and the notch sensitivities were lower.

Figure 10(a) shows a typical SEM image of a fatigue crack on a notch root surface of steel D failed at $N_f = 5.0 \times 10^4$ cycles. The fatigue crack is originated mainly in the wide lath-martensite structure. Also, propagation of the crack is disturbed by the M-A like phase. In this case, inclusions such as Al_2O_3 are not likely to be crack initiation sites at the surface in the current study (Fig. 10(b)).

Fig. 6. Variations in (a) initial volume fraction ($f_{\gamma 0}$) and carbon concentration ($C_{\gamma 0}$) of retained austenite and (b) volume fractions of M-A like phase (f_{M-A}) and carbide (f_θ) as a function of carbon content (C) in steels A–E.
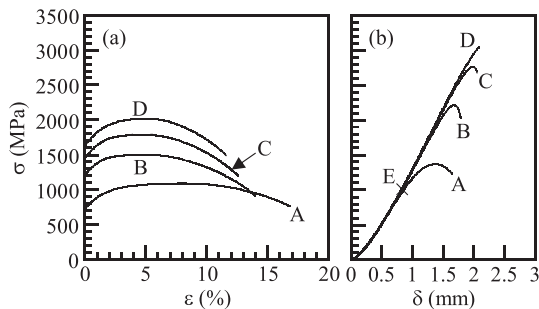

Fig. 7. (a) Nominal stress-plastic strain (σ-ε) curves of smooth specimens and (b) nominal stress-displacement (σ-δ) curves of notched specimens in steels A–E.

Table 2. Vickers hardness, tensile properties, and fatigue properties of steels A–E.

Steel	HV	YS	TS	TS_N	NSR	UEl	TEl	LEl/TEl	FL	FL_N	q
A	284	713	1 046	1 338	1.28	7.3	17.0	0.57	847	453	1.24
B	457	1 193	1 495	2 214	1.48	3.7	14.0	0.74	969	645	0.72
C	535	1 448	1 786	2 771	1.55	3.4	12.8	0.73	1 141	807	0.59
D	600	1 620	2 009	3 042	1.51	4.0	11.7	0.66	1 300	847	0.77
E	717	1 830	1 845	874	0.47	0.0	0.0	0.00	1 067	619	1.03

HV: Vickers hardness number; *YS* (MPa): 0.2% offset proof stress or yield strength; *TS* (MPa): tensile strength; *TS*$_N$ (MPa): notch-tensile strength; *NSR*: notch-tensile strength ratio; *UEl* (%): uniform elongation; *TEl* (%): total elongation; *FL* (MPa): fatigue limit of smooth specimen; *FL*$_N$ (MPa): fatigue limit of notched specimen; *q*: notch-sensitivity factor; *: not measured.
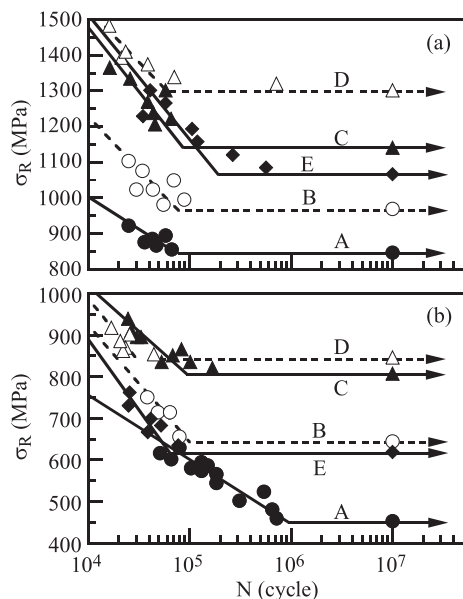
Fig. 8. Stress amplitude-number of cycles (*S-N*) curves of (a) smooth and (b) notched specimens in steels A–E.
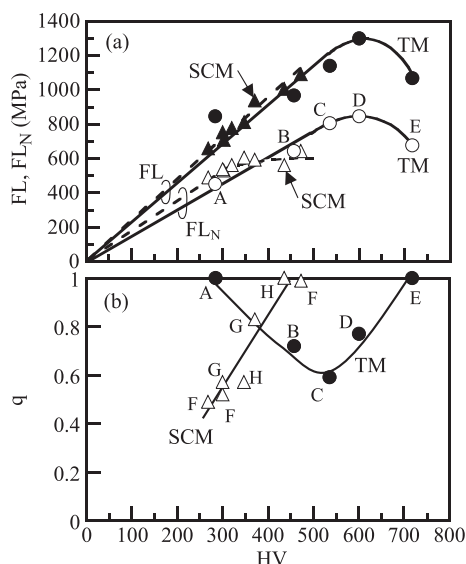

Fig. 9. Variations in (a) fatigue limits (*FL*, *FL*$_N$) and (b) notch sensitivity (*q*) of smooth and notched specimens as a function of Vickers hardness (*HV*) in steels A–E (○ ●; TM) and steels F–H (△ ▲; SCM).

4. Discussion

4.1. Microstructure and Retained Austenite Characteristics of Steels B–D

According to Kobayashi *et al.*,[9] the microstructural changes in TM steels subjected to an ITP process at temperatures lower than the M_f temperature can be illustrated as shown in **Fig. 11**(d), and summarized as follows.

Stages 1–3: When the steel is cooled to a T_3 temperature lower than the M_s temperature, the austenite first transforms to a wide lath-martensite structure (stages 2–3 in Figs. 11(a), 11(c) and 11(d)). In this stage, carbide does not precipitate in the wide lath-martensite structure. According to Koistinen and Marburger,[19] the amount of wide lath-
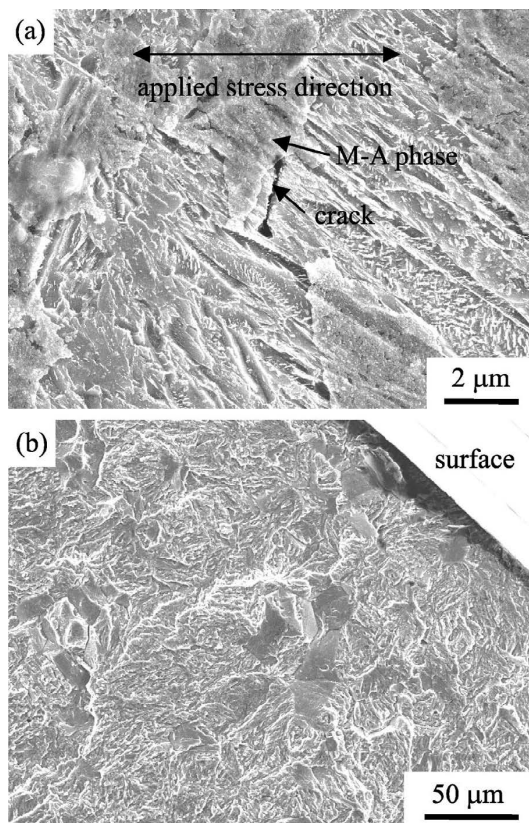

Fig. 10. Scanning electron microscopy images of (a) initial crack and (b) failure surface of notched specimen in steel D, fractured at $N_f = 5.0 \times 10^4$ cycles.

martensite structure ($f\alpha_m$) is given by the following equation,

$$f\alpha_m = 1 - \exp\{-A(M_S - T_3)^B\} \dots\dots\dots (3)$$

where A and B are material's constants.

Stages 3–5: On subsequent continuous cooling to the isothermal transformation temperature ($T_{IT} = 50°C$) below the M_f temperature, the wide lath-martensite structure is auto-tempered, that is, a small amount of carbide precipitates only in the wider lath-martensite structure. Simultaneously, some supersaturated solute carbon diffuses into the untransformed austenite. Then, most of the untransformed austenite is transformed into a narrow lath-martensite structure, with a little retained austenite on the lath boundary (stages 3–5 in Figs. 11(c) and 11(d)). No carbide precipitates in the narrow lath-martensite structure.

Stages 5–7: During isothermal transformation holding, supersaturated solute carbon in wide and narrow lath-martensite structures diffuses into the retained austenite (stages 5–7 in Fig. 11(d)).

Stages 8–11: The retained austenite phase is further carbon-enriched by diffusion of supersaturated carbon in the wide and narrow lath-martensite structures, without further carbide precipitation in these lath-martensite structures and a decrease in the retained austenite volume fraction.

As shown in Figs. 4 and 6 and Table 2, the volume fraction of the M-A like phase increased with increasing carbon content in steels B–D, with refining of the wide lath-martensite structure and a small increase in the retained austenite fraction. The carbon concentration of the retained austenite and
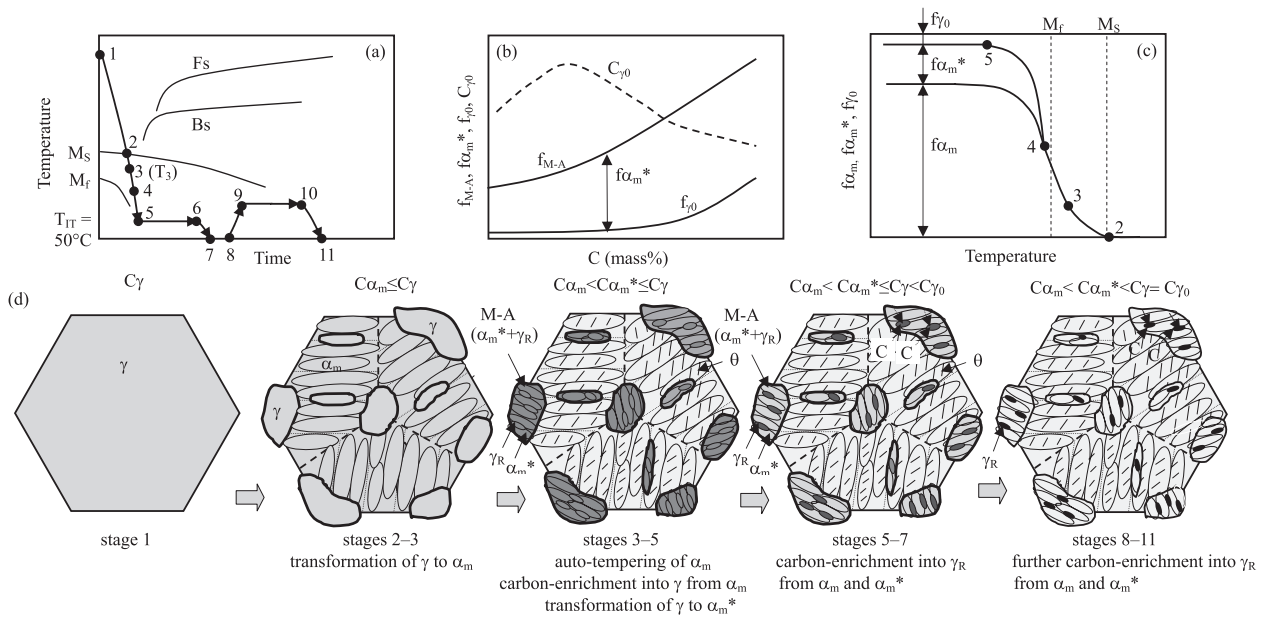
Fig. 11. Illustration of (a) heat treatment diagram, (b) carbon content dependences of initial volume fraction ($f\gamma_0$) and carbon concentration ($C\gamma_0$) of retained austenite and volume fractions of M-A (f_{M-A}) and narrow lath-martensite ($f\alpha_m^*$), (c) variations in martensitic transformation volume ($f\alpha_m$), $f\alpha_m^*$ and $f\gamma_0$ with temperature and (d) microstructural changes at stages 1–11 during heat treatment in steel D, in which α_m, α_m^*, γ, γ_R, M-A and θ represent wide lath-martensite, narrow lath-martensite, austenite, retained austenite, M-A like phase and carbide, respectively. $C\gamma$, $C\alpha_m$ and $C\alpha_m^*$ are carbon concentrations of austenite, wide lath-martensite and narrow lath-martensite, respectively.

carbide fractions became maximum in steels B and C. In general, the higher the carbon content (the lower the *M*s temperature) of a steel, the greater the increase in the volume fraction of untransformed austenite, accompanied by a subsequent increase in the M-A like phase fraction (Fig. 11(b)), as well as a decrease in the carbide fraction in the wide lath-martensite. This may control the volume fraction of the M-A like phase in steels B–D, leading to a high carbon concentration in the retained austenite and carbide fractions in steels B and C. The decreased carbon concentrations of the retained austenite in steels D and E may be influenced by transformation expansion strain of narrow lath-martensite surrounding the retained austenite, which reduces the lattice constant of the retained austenite.

4.2. Low Notch-Tensile Strength Ratios of Steels B–D

According to Majima *et al.*,[20] the notch-tensile strength ratio of a ductile metal is mainly controlled by two primary factors, namely (i) the stress triaxiality factor and (ii) the ratio of local elongation to total elongation (*LEl/TEl*). The larger the values of these two factors, the higher the notch-tensile strength ratio because of an increase in plastic notch constraint. **Figure 12**(a) shows the notch-tensile strength ratios of steels A–D and steels F–H as a function of *LEl/TEl*, with those of 0.2%C-1.5%Si-1.5%Mn-0–1.0%Cr-0–0.2%Mo-0–1.5%Ni-0.05%Nb TBF steels.[17] In the figure, these notch-tensile strength ratios tend to increase with increasing *LEl/TEl*, although steel A exhibits a lower notch-tensile strength ratio. So, it is considered that the higher notch-tensile strength ratios of steels B–D are caused by larger *LEl/TEl* values under a constant stress triaxiality factor, similar to steels F–H and the TBF steels.

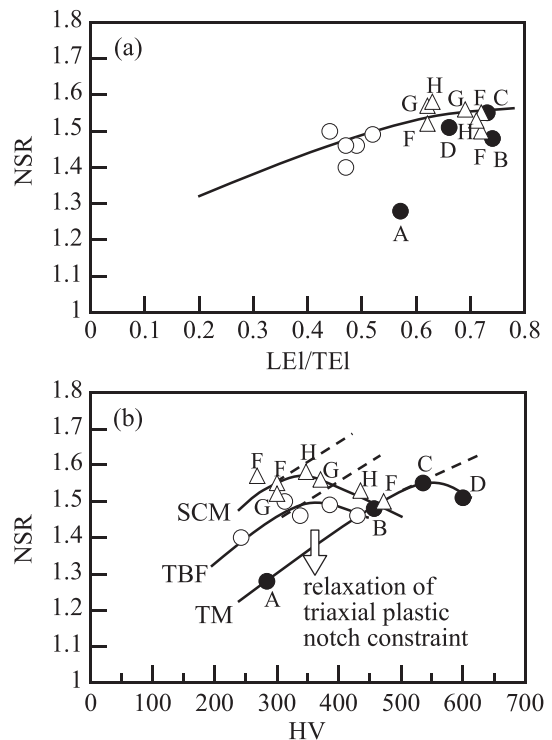If the above-mentioned notch-tensile strength ratios are plotted as a function of Vickers hardness, steels A–D belong

Fig. 12. Relationships between notch-strength ratio ($NSR = TS_N/TS$) and (a) *LEl/TEl* and (b) Vickers hardness (*HV*) in steels A–D (●; TM), 0.2%C-1.5%Si-1.5%Mn-0–1.0%Cr-0–0.2%Mo-0–1.5%Ni-0.05%Nb TRIP-aided bainitic ferrite steels (○; TBF) and steels F–H (△; SCM).

to a group with lower notch-tensile strength ratios than steels F–H, in the same way as for the TBF steels (Fig. 12(b)). This result indicates that the retained austenite in the M-A like phase plays a role in reducing the notch-tensile strength ratio through a plastic relaxation of the strain-

induced transformation to martensite, as well as the softened wide lath-martensite, which increases the uniform elongation or decreases local elongation. In other words, it is expected that the strain-induced transformation of the retained austenite effectively relaxes triaxial plastic notch constraint in steels B–D.

4.3. High Notch-Fatigue Limits of Steels B–D

In general, the notch-fatigue limit of a conventional ultra-high-strength structural steel is saturated in the high Vickers hardness range, as shown in steels F–H (Fig. 9(a)). However, the notch-fatigue limits of steels B and D linearly increased with Vickers hardness, even in the Vickers hardness range between HV457 and HV600.

In section 4.2, it was suggested that the strain-induced transformation of the retained austenite plastically relaxes a triaxial plastic notch constraint in steels B–D, compared with steels F–H. In addition, the growth of fatigue cracks was disturbed by the blocky M-A like phase, as shown in Fig. 10(a). According to Knott,[21] the plastic zone size (d_Y) at a small crack tip can be estimated using the following equation,

$$d_Y = K^2/(3\pi YS^2) \quad \text{............................ (4)}$$

where K is the stress intensity factor, defined by $\sigma(\pi c)^{1/2}$, σ is the applied stress, and c is the crack length. In steel D, the plastic zone size is estimated to be about 4.0 μm if the fatigue crack length at the first stage is $2c = 30$ μm, equivalent to the prior austenitic grain size, and the applied stress is the maximum stress ($\sigma = \sigma_{max} = FL/0.9 = 1\,444$ MPa), corresponding to the fatigue limit. The plastic zone always includes some retained austenite particles in M-A like phase (see **Fig. 13**) because the interparticle path of M-A like phase is 0.5–2.0 μm (Fig. 4(b)). Therefore, the plastic relaxation by the strain-induced transformation of retained austenite can be expected to take place always in the plastic zone during fatigue deformation. From these facts and the metallurgical characteristics of steels B–D, it is considered that the followings contribute to the high notch-fatigue limit and low notch sensitivity through the suppression of crack initiation and propagation in steels B–D:

(1) a plastic relaxation of localized stress concentration as a result of the strain-induced transformation of 3–5 vol% metastable retained austenite;

(2) a large amount of finely dispersed M-A like phase along prior austenitic, packet and block boundaries;

(3) a small amount of carbide, precipitated only in the wide lath-martensites structure

In (1), the transformed martensite also decreases the triaxial plastic notch constraint and plays a role in suppressing crack initiation and propagation. Regarding (2), a difference in flow stress between the wide lath-martensite structure and the M-A like phase may produce a high compressive long-range internal stress in the wide lath-martensite structure matrix, suppressing crack initiation.[22] Factor (3) decreases the number of crack initiation cites and therefore suppresses crack initiation.

According to previous studies,[8,11] the mechanical stability of retained austenite in TM steels is hardly influenced by the carbon concentration, because most of the retained austenite phases are surrounded or constrained by hard narrow
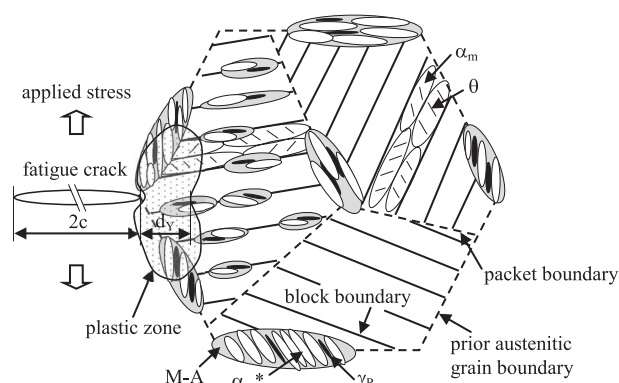

Fig. 13. Illustration of plastic zone size (d_Y) in steel D at crack tip and distribution of M-A like phases; α_m, α_m^*, γ_R and θ represent wide lath-martensite, narrow lath-martensite, retained austenite and carbide, respectively.

lath-martensite structures. So, a high volume fraction of retained austenite in steels B–D may further increase the contribution of (1) to fatigue deformation.

5. Conclusions

The notch-fatigue strengths and notch sensitivities of 0.1–0.6%C-1.5%Si-1.5%Mn TM steels were investigated for automotive applications. Also, the notch-fatigue properties were related to the microstructural and retained austenite characteristics. The main results are summarized as follows.

(1) If TM steels containing 0.2%, 0.3% or 0.4%C were subjected to an ITP process, consisting of isothermal transformation and partitioning processes, they achieved much higher notch-fatigue limits and lower notch sensitivities than conventional 0.2–0.4%C-1.0%Cr-0.2%Mo structural steels without retained austenite.

(2) It was expected that high notch-fatigue limits were principally associated with (i) plastic relaxation of localized stress concentration as a result of the strain-induced transformation of 3–5 vol% metastable retained austenite and (ii) a large amount of finely dispersed M-A like phase along prior austenitic, packet and block boundaries, as well as (iii) a small amount of carbide only in the wide lath-martensite structure, which contribute to difficult fatigue crack initiation and/or propagation.

REFERENCES

1) T. Furukawa: *Mater. Sci. Technol.*, **5** (1989), 465.
2) U. Brux, G. Frommeyer, O. Grassel, L. W. Meyer and A. Weise: *Steel Res.*, **73** (2002), 294.
3) W. Cao, J. Shi, C. Wang, L. Xu, M. Wang and H. Dong: Proc. of ICAS 2010, Metall. Ind. Press, Beijing, (2010), 196.
4) J. G. Speer, D. V. Edmonds, F. C. Rizzo and D. K. Matlock: *Solid State Mater. Sci.*, **8** (2004), 219.
5) K. Sugimoto, J. Sakaguchi, T. Iida and T. Kashima: *ISIJ Int.*, **40**

(2000), 920.

6) K. Sugimoto, M. Murata and S. M. Song: *ISIJ Int.*, **50** (2010), 162.

7) K. Sugimoto and J. Kobayashi: Proc. of MS&T '10, TMS, Warrendale, PA, (2010), 1639.

8) J. Kobayashi, D. V. Pham and K. Sugimoto: *Steel Res. Int.* (Special Edition; ICTP2011), (2011), 598.

9) J. Kobayashi, S. M. Song and K. Sugimoto: *ISIJ Int.*, **52** (2012), 1124.

10) K. Sugimoto, D. Ina and J. Kobayashi: Proc. of ICAS 2010, Metall. Ind. Press, Beijing, (2010), FR004, 14, (CD-R).

11) J. Kobayashi, D. Ina and K. Sugimoto: Proc. of MS&T'12, TMS, Warrendale, PA, (2012), 937.

12) I. Tamura: Strength of Steels, Nikkan Kogyo Shinbunn, Tokyo, (1970), 40.

13) H. Maruyama: *J. Jpn. Soc. Heat Treat.*, **17** (1977), 198 (in Japanese).

14) D. J. Dyson and B. Holms: *J. Iron Steel Inst.*, **208** (1970), 469.

15) O. Umezawa: *J. Jpn. Inst. Light Met.*, **50** (2000), 86 (in Japanese).

16) C. Wang, Y. Zhang, W. Cao, J. Shi, M. Wang and H. Dong: *Sci. China Technol. Sci.*, **55** (2012), 1844.

17) N. Yoshikawa, J. Kobayashi and K. Sugimoto: *Metall. Mater. Trans. A*, **43** (2012), 4129.

18) G. E. Dieter: *Mechanical Metallurgy* (SI Metric Edition), McGraw-Hill Book Co., London, (1988), 403.

19) D. P. Koistinen and R. E. Marburger: *Acta Metall.*, **7** (1959), 59.

20) T. Majima, M. Anzai and H. Nakazawa: *Trans. Jpn. Soc. Mech. Eng. A*, **52** (1986), 117 (in Japanese).

21) J. F. Knott: Fundamentals of Fracture Mechanics, Baifukan, Tokyo, (1977), 127.

22) K. Sugimoto, M. Kobayashi and S. Hashimoto: *Metall. Trans. A*, **23A** (1992), 3085.